A methodology for the structural design of LiftWEC: A wave-bladed cyclorotor

Abel Arredondo-Galeana, Weichao Shi, Gerrit Olbert, Martin Scharf, Andrei Ermakov, John V. Ringwood and Feargal Brennan

***Abstract*—Novel wave energy convertors (WECs) need to be designed to ensure both longevity and hydrodynamic efficiency. Hence there is a need to develop methodologies that tackle both the hydrodynamic and structural requirements of WECs. Here we demonstrate an integral methodology for the design of LiftWEC: a two-foil wave bladed cyclorotor. The hydrofoils follow the orbital motion of the wave particles and rotate around a central axis. The span of the hydrofoils is aligned to the crest of the wave, making the device a wave terminator, i.e. a device that cancels the incoming wave. The phase of the rotation is different to that of the incoming wave. This phase difference generates lift and sustains the rotation of the hydrofoils. In this paper, a low-order two-dimensional hydrodynamic model and a structural model based on beam theory are weakly coupled to assess power production and structural stresses on the device. We estimate the forces on the hydrofoils due to regular waves under design conditions. By studying two rotor configurations and two typical loading cases on the hydrofoils, we demonstrate that LiftWEC is structurally resilient to design conditions. We show that, for the selected wave design conditions, the optimum radius to span ratio is about 0.8, which ensures maximum mean power output, but also, a reduced structural penalty. We therefore demonstrate a powerful design tool and pave the way for future frequency analysis studies for this type of devices.**

***Index Terms*—Wave bladed cyclorotor, WEC, linear wave theory, beam theory, bending moments, hydrofoils.**

I. Introduction

Wave energy is approaching rapidly a commercial stage. Lessons learnt, such as decreasing installation and maintenance costs, developing strong and cheap materials and avoiding racing through the technology readiness level (TRL) scales [1], together with governmental support schemes, are fomenting the growth of the sector. Simultaneously, offshore oil and gas and offshore multi-platforms are scaling up investments into low-carbon technologies [2]. This fosters a promising scenario for wave energy developers as major opportunities lie on the horizon. Development of wave energy, however, comes with major challenges as well, and efforts in areas involving innovation, design, operation and maintenance, are needed.

Wave energy converters (WECs) are technology diverse and have not converged into one type of technology. This diversity, however, makes wave energy versatile to suit different wave conditions and locations. In fact, several ways of classification for WECs exist. One method for example, is according to their working principle [3], [4]. For example, they can be: oscillating water columns, overtopping devices, heaving buoys, submerged pressure differential devices, wave activated bodies, bulge wave devices, oscillating wave surge converters, rotating mass devices and wave bladed cyclorotors.

Typically, the hydrodynamics and structural requirements of WECs are unique and analogies in other industries are difficult to find [5]. In contrast, wave-bladed cyclorotors utilise foils to generate lift. Vast information on foils exist in the literature [6] and they are utilised for energy extraction in horizontal and vertical wind turbines [7], horizontal tidal turbines [8], with ubiquitous use in helicopters [9], propellers [10] and a wide variety of rotating devices. This presents an advantage for wave bladed cyclorotors, where operation design knowledge is transferable from other industries, as opposed to other types of WECs where knowledge transfer is more challenging.

Research into wave bladed cyclorotors started in the 90s with single hydrofoil devices. The hydrofoils rotated around an axis parallel to the crest of the incoming waves [11], [12]. Chaplin and Retzler [13] proposed the use of spinning cylinders to generate lift, with the Magnus effect, therefore eliminating the need to specify an angle of attack. More than a decade later, the wave cancellation properties of a two foil wave cyclorotor were explored in regular waves [14], [15] and in irregular waves [16]–[18]. Later on, the efficiency of the device was measured in three dimensional oblique waves [19], [20]. In recent years, a benchmark study for a wave bladed cyclorotor was conducted by Siegel [21], showing great energy capture potential for this type of device, and Folley and Whittaker [22] also presented an analysis of the potential benefits of lift-based WECs.

Most of these studies have focused on the far field hydrodynamics of wave-bladed cyclorotors, with emphasis on capturing wave cancellation downstream of model-scale cyclorotors. However, less effort has been given to the near field hydrodynamics and to the structural design of wave-bladed cyclorotors. In fact, to the best knowledge of the authors, a documented hydro-structural methodology for wave-bladed cyclorotors is

This work was supported by the European Union's Horizon 2020 Research and Innovation Programme under Grant Agreement No 851885.

A.A.G, W.S. and F.B are with the Department of Naval Architecture, Ocean and Marine Engineering at the University of Strathclyde, Glasgow, UK, (e-mail: abel.arredondo-galeana@strath.ac.uk, weichao.shi@strath.ac.uk, feargal.brennan@strath.ac.uk)

G.O.and M.S. are with Institute for Fluid Dynamics and Ship Theory, Hamburg University of Technology, Hamburg, Germany, (e-mail: gerrit.olbert@tuhh.de, martin.scharf@tuhh.de)

A.E. and J.V.R. are with Centre for Ocean Energy Research, National University of Ireland Maynooth, Ireland, (e-mail: andrei.ermakov@mu.ie, john.ringwood@mu.ie)

missing from the literature. Hence, there is a need to develop a clear methodology that integrates the near field hydrodynamic and structural requirements of this type of device. This will help in the design of large scale wave cyclorotors and open novel design strategies based on frequency-domain analysis. Here, we consider the case of LiftWEC, a wave-bladed cyclorotor considered to have two nominal foils for the purpose of this study. We develop a holistic methodology that considers the near field hydrodynamics and the structural requirements of this type of device.

The structure of this paper is as follows. First, we introduce the wave-bladed cyclorotor: LiftWEC. Secondly, we present the wave design conditions and the hydrodynamic model. The structural model is then developed based on first principles of beam theory. The models are coupled and results are shown for the hydrofoils subject to different types of loading. Finally, guidance is given in terms of dimensioning the device for optimum power extraction and reduced structural penalty, and we set the way forward towards studies of fatigue and structural dynamics of wave bladed cyclorotors.

II. Methodology

A. The LiftWEC concept

The LiftWEC wave-bladed cyclorotor is shown in figure 1. The rotor consists of two hydrofoils connected to a central shaft by radial spokes. The support structure, for the purposes of this study, is assumed to consist of two v-frames that are connected to the central shaft by means of roller bearings.

The hydrofoils, of uniform cross-section along the span s, rotate following the wave orbital motion. The phase of the rotation is controlled so that it is different to that of the incoming wave. This phase difference $\Delta\varphi$ generates an inflow velocity w at an angle of attack α and hence a lift force in the hydrofoils. Provided that α does not exceed the stall angle of the hydrofoils (α_s), the tangential component of the lift force sustains the rotation motion of the device. A side-view of a cyclorotor with two hydrofoils, labelled hydrofoil 1 and hydrofoil 2, showing w and α on each hydrofoil, and $\Delta\varphi$ in hydrofoil 1, is shown in figure 2.

LiftWEC is conceptually designed to operate in the Atlantic coast of France. According to Sierra et al. [23], most of the energy in this region is concentrated in sea states with wave periods (T_p) between 10 to 12 s and significant wave heights (H_s) between 2 and 4 m. As such, in this paper, we consider the design sea state to be $T_p = 10\,\mathrm{s}$ and $H_s = 4\,\mathrm{m}$.

B. Hydrodynamic modelling

By considering large span hydrofoils, we can assume two-dimensional flow. Hence the lift and drag forces on a hydrofoil are given by

$$F_L = \frac{1}{2}\rho w^2 s c C_L \tag{1}$$

and

$$F_D = \frac{1}{2}\rho w^2 s c C_D, \tag{2}$$

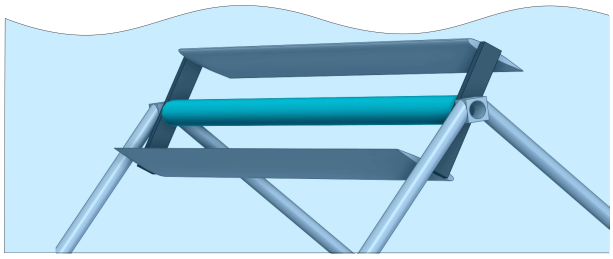

Fig. 1. LiftWEC wave bladed cyclorotor in operation near the water surface and supported by two v-frames

where ρ is the fluid density, w is the relative velocity of the incoming flow, s is the span of the hydrofoil, c is the chord length and C_L and C_D are the lift and drag force coefficients.

Figure 2 shows the side view of a LiftWEC rotor at the normalised time period $t/T_p = 0$. The wave direction is from left to right and the wave particle motion is clockwise [24]. Hence the rotation of the rotor follows the clockwise wave particle motion. The rotor has a submergence μ measured from the mean sea level to the zenith of the rotor's orbital path. The wave velocity component is v, whilst u is the negative of the tangential velocity of the hydrofoils.

At $t/T_p = 0$, the angular position of the rotor (θ) is set to $\theta = 0°$. The angle is measured between the radial strut of hydrofoil 1 and the horizontal positive x-axis. The wave crest is parallel to the rotating axis of the rotor and v points into the wave direction. The phase difference $\Delta\varphi$ is measured between u and v of the two hydrofoils. In figure 2, $\Delta\varphi = +90°$ for hydrofoil 1 and $\Delta\varphi = -90°$ for hydrofoil 2.

As stated previously and as shown in figure 2, $\Delta\varphi$ generates w and α on the hydrofoils. This in turns generates a lift and a drag force F_L and F_D, respectively. These force components can be transformed into tangential (F_T) and radial (F_R) forces acting on the hydrofoils, as given later by equations 11 and 12, respectively. The tangential component F_T sustains the rotation of the rotor, whilst F_R causes the bending moments in the hydrofoils.

We introduce now the equations of the hydrodynamic model. Consider a rotor of radius r. Then the position of the hydrofoils, which are considered punctual, is given by

$$x = r\cos(\theta(t) + \psi) \tag{3}$$

and

$$z = z_0 + r\sin(\theta(t) + \psi), \tag{4}$$

where $\theta(t)$ is the angular position with respect to the positive horizontal axis and ψ is the initial angular position of each hydrofoil, measured also from the positive horizontal axis. For hydrofoil 1, $\psi = 0°$ and for hydrofoil 2, $\psi = 180°$. In equation 4, $z_0 = -(\mu + r)$.

The tangential velocity components (u_x, u_y) of the hydrofoils are obtained by deriving equations 3 and 4, such that

$$u_x = -\omega r\sin(\theta(t) + \psi) \tag{5}$$

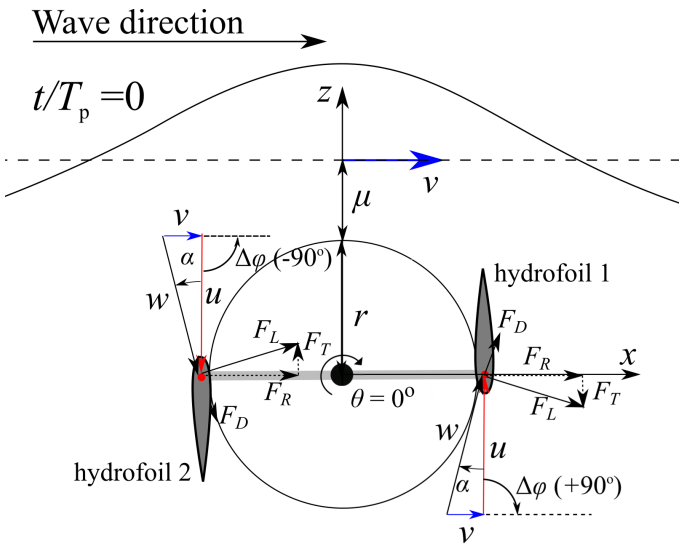

Fig. 2. Side view of a LiftWEC rotor showing the lift and drag forces (F_L, F_D) on hydrofoils, the wave velocity v, the velocity due to the rotation of the hydrofoils u, the relative velocity w and the phase difference $\Delta\varphi$ at $t/T_p = 0$

and

$$u_y = \omega r \cos(\theta(t) + \psi), \tag{6}$$

where ω is a constant rotational frequency and is equal to the angular frequency of the incoming monochromatic wave.

For intermediate water depths, the wave velocity components are computed with Airy linear wave theory [25], such that

$$v_x = \frac{\omega H}{2} \frac{\cosh(k(z+h))}{\sinh(kh)} \cos(kx - \omega t) \tag{7}$$

and

$$v_y = \frac{\omega H}{2} \frac{\sinh(k(z+h))}{\sinh(kh)} \sin(kx - \omega t), \tag{8}$$

where H is the wave height, k is the wave number, h is the water depth, x and z are the horizontal and vertical positions of the hydrofoils, as defined by equations 3 and 4, respectively. The wave number k is computed with the intermediate water depth dispersion relationship [26] and is equal to $k = 0.063$.

The relative velocity $\boldsymbol{w}$ on the hydrofoils is the vectorial sum of the wave velocity component $\boldsymbol{v}$ and the negative of the tangential velocity of the hydrofoils $\boldsymbol{u}$, such that

$$\boldsymbol{w} = \boldsymbol{v} - \boldsymbol{u}, \tag{9}$$

as shown in the vector diagrams of figure 2.

For this study, we consider symmetric NACA0012 profiles with a zero pitch angle. The corresponding lift and drag coefficients (C_L, C_D) are obtained from Klimas and Sheldhal [27] for a range of α between $-180°$ to $180°$. From figure 2, α is computed by taking the inverse of the sine of the cross product of $\boldsymbol{w}$ and $\boldsymbol{u}$, and dividing it by the product of their Euclidian norm, such that

$$\alpha = \sin^{-1}\left[\frac{||w \times u||}{||w||||u||}\right]. \tag{10}$$

Subsequently, a look up table is utilised to obtain C_L and C_D. Finally, by defining s and c and utilising equations 1 and 2, F_L and F_D can be determined. The tangential force in the hydrofoils is defined as

$$F_T = F_L \sin\alpha - F_D \cos\alpha \tag{11}$$

and the radial force is

$$F_R = F_L \cos\alpha + F_D \sin\alpha. \tag{12}$$

Because F_T is dependent on the angular position (θ), the average tangential force is expressed as:

$$\overline{F_T} = \frac{1}{2\pi} \int_0^{2\pi} F_T(\theta) d\theta. \tag{13}$$

The total torque (Q) is

$$Q = rN\overline{F_T}, \tag{14}$$

where N is the number of hydrofoils in the rotor. Finally, the power output can be computed as

$$P = Q\omega. \tag{15}$$

C. Angle of attack oscillations (α)

We note that the hydrodynamics of this type of rotor are similar in nature to cross-flow turbines (both wind and water), where there exists vast research on dynamic stall - a rotor's ability to maintain lift through severe angles of attack through blade/vortex interactions [8]. In figure 3, we present the angle of attack oscillations (α) throughout one period of revolution at $\Delta\varphi = 90°$ for hydrofoil 1. Although in this example, the amplitude of α is not severe, dynamic stall is likely to occur under different wave conditions. Hence, further iterations of the model will consider dynamic stall effects.

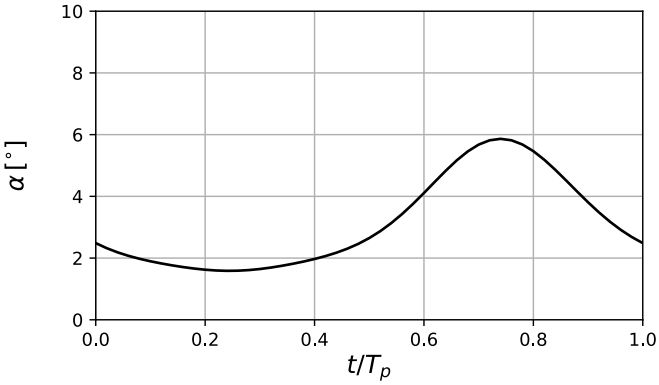

Fig. 3. Angle of attack oscillations (α) in hydrofoil 1 for one period of revolution at design sea state conditions.

III. Structural Considerations

A. Hydrofoil material and cross-section

A moderate strength steel, used for offshore applications [28], is selected as the construction material. The mechanical properties of the selected steel are listed in table I. In the table, the allowable stress level is defined as one third of the yield stress level (σ_y). We

note, however, that different thresholds can be selected according to design requirements.

The hydrofoil is modelled with a square hollow section (SHS). This is a simplification of the actual hydrofoil cross-section, which is shown in figure 4. The cross-section is representative of the wing box, which is the main structural component of the hydrofoil and of any wing [29]. Modelling the hydrofoil as a SHS allows the structural design to be based on first principles and it enables coupling of the structural model to the hydrodynamic model in a computationally inexpensive manner. In figure 4, each side of the SHS is $0.12c$, where c is the chord of the hydrofoil.

TABLE I
MECHANICAL PROPERTIES OF MODERATE STRENGTH OFFSHORE STEEL

Property	Threshold (MPa)
Yield stress (σ_y)	350
Ultimate strength (σ_u)	410
Allowable stress (σ_a)	117

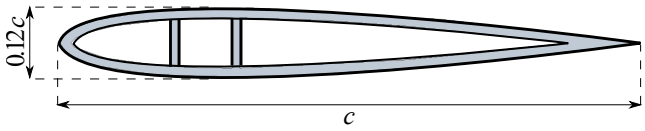

Fig. 4. Hydrofoil cross-section of NACA 0012, with square hollow section (SHS) used in the structural model. The SHS is made of steel, which is the same material utilised for the suction and pressure walls of the foil.

B. LiftWEC configurations - fixed and cantilever beam

Two prototype configurations for LiftWEC are analysed: One where the hydrofoils are supported at both ends (figure 5a), and one where the hydrofoil is supported in the middle only (figure 5b). We refer to these configurations, as the fixed and cantilever beam configurations, respectively. Both configurations have two hydrofoils and are supported by two bottom fixed v-frames attached to the seabed. The main substructures of the device are shown in figure 5, namely the hydrofoils, spokes, support structure, central shaft and power take-off (PTO). The hydrofoils are the substructures that are subject to the highest bending stresses and therefore are more susceptible to failure. Hence, we focus the structural analysis on these substructures.

C. Loading distribution on hydrofoils

For a LiftWEC device of large span, we expect two-dimensional flow and uniform loading. However, for small spans, three dimensional effects (tip vortices, spanwise flow, etc.) may play a more significant role and non-uniform loading might occur on the hydrofoils. As an example, figure 6 shows the surface of a hydrofoil subject to different types of loading. In the figure, the vertical axis shows the normalised distributed load, which is referred to as non-dimensional distributed load, whilst the horizontal axis shows the

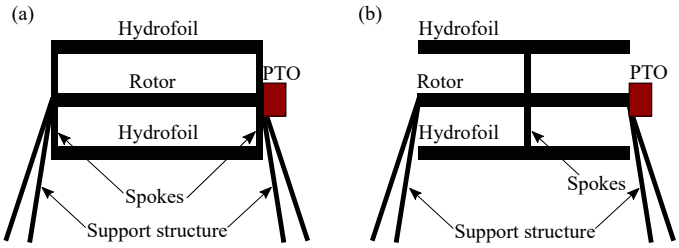

Fig. 5. a) LiftWEC rotor with hydrofoils supported at both ends (fixed beam configuration) and b) LiftWEC rotor with hydrofoils supported in the middle and with free ends (cantilever beam configuration).

non-dimensional span of the hydrofoil. Uniform, elliptical, quadratic and linear types of loading are shown with solid, dashed, starred and dotted-dashed lines, respectively. We recall that uniform an elliptical loading are typical loading examples of large-span and elliptical wings, respectively. Quadratic and linear loadings are geometrical approximations of more complex types of loading [30] that could occur due to three-dimensional effects.

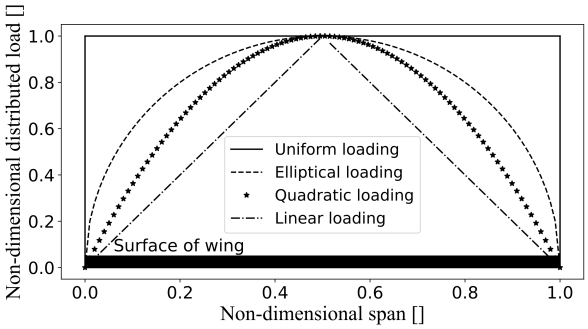

Fig. 6. Different types of loading on the surface a hydrofoil: uniform (solid line), elliptical (dashed line), quadratic (starred line) and linear (dotted-dashed line). In the figure, the horizontal axis is the non-dimensional span and the vertical axis is the non-dimensional distributed load.

We utilise uniform and linear loading as two representative extreme cases of loading. We assume that uniform loading is the envelope for two-dimensional flow, with linear loading the one relevant for three-dimensional flow. We will then compute the shear forces (V), bending moments (M) and deflections (z) over hydrofoils of a given span.

D. Structural model

The structural model is introduced in this subsection. Figures 7a and 7b show uniform and linear loading applied to the fixed and cantilever beam configurations, respectively. The origin in the y-axis ($y = 0$) is defined in both of the subfigures. Different reference systems are used for each of the beam configurations, because typically, the full length of the cantilever beam, is considered from fixed-end to free-end, whilst in fixed beams, the full length is considered from fixed-end to fixed-end. We note, however, that the reference systems could be modified to be the same for both rotor configurations.

1) Uniform loading UL: The total force F acting on the hydrofoil of the fixed beam configuration under uniform loading is F_R, as defined previously in equation 12. In the cantilever beam configuration, F is half of that computed with equation 12, because the structural model depicts just half of the length of the hydrofoil (figure 7b). We can distribute F uniformly along the length of the hydrofoil, such that

$$w_0 = \frac{F}{l}, \tag{16}$$

where w_0 is the distributed load and l is the length of the hydrofoil as specified in figures 7a and 7b. For uniform loading, w_0 is constant along the y-axis. Hence the local distributed load w_y is equal to w_0. Consequently, we can define the local force F_y, such that

$$F_y = w_y y, \tag{17}$$

where y is defined within the range $0 \leq y \leq l$, as specified in figures 7a and 7b.

2) Linear loading LL: In this case, the local distributed load w_y changes with y. Hence, for the fixed beam configuration

$$w_y = \frac{2w_0 y}{l}, \tag{18}$$

in the interval of $0 \leq y \leq l/2$ and for the cantilever configuration

$$w_y = \frac{w_0 y}{l}, \tag{19}$$

in the interval of $0 \leq y \leq l$.

The equivalent local force F_y, in the fixed beam configuration is computed by calculating the area of a triangle of base y and height w_y, such that

$$F_y = \frac{w_0 y^2}{l}, \tag{20}$$

over the range $0 \leq y \leq l/2$. In contrast, for the cantilever beam configuration,

$$F_y = \frac{w_0 y^2}{2l}, \tag{21}$$

over the range $0 \leq y \leq l$.

We can now compute F_y, with equations 17, 20 or 21, depending on the type of loading (uniform, linear) and type of configuration (fixed, cantilever). The point of action of F_y is the centroid of the area delimited by the type of loading. For a rectangular shape (uniform loading), the centroid is at the symmetry line. For a right-angled triangle (linear loading), the centroid is located at a $1/3^{rd}$ distance from the right angle.

As an example, the centroid of the equivalent load between $y = 0$ and $y = l/2$, in the fixed beam configuration, and the centroid of the equivalent load between $y = 0$ and $y = l$, in the cantilever beam configuration, are shown as circular black markers in figure 7a and figure 7b, respectively.

3) Shear forces, bending moments and deflections: The local forces F_y and the centroid locations defined in the $y-$axis are utilised in the free body diagrams to solve for the shear forces (V) and bending moments (M). The cantilever beam configuration is a determinate problem and V and M can be solved with the static equilibrium equations. In contrast, the fixed beam configuration is an indeterminate problem, and the problem is solved with a further equation. The additional equation is the general differential equation of the elastic curve:

$$EI\frac{d^2 z}{dy^2} = M, \tag{22}$$

where M is the bending moment, E is the elastic modulus of the material, and I is the second moment of area of the cross-section. Equation 22 is integrated twice and solved for z by defining a couple of boundary conditions, the maximum or minimum deflection, and the zero displacement point of the beam. Maximum or minimum deflection occurs at midspan in the fixed beam configuration, whilst zero deflection occurs at the fixed ends of the beam.

The procedure described above can be applied to different types of loading by recomputing equations 18, 19, 20 and 21. Table II summarises the solutions for V, M and z for LL for fixed and cantilever beam configurations. For UL, solutions can be found in structural mechanics text books [31]. The results of the LL equations of table II and the UL equations, were validated with online solvers SkyCiv and ClearCalcs.

4) Bending stresses: For both fixed and cantilever cases, the maximum bending stresses occur at the most distant point from the neutral axis of the beam cross-section [32] and is given by

$$\hat{\sigma} = \frac{\hat{M}\hat{z}}{I}, \tag{23}$$

where $\hat{M}$ is the maximum bending moment, $\hat{z}$ is the distance from the neutral axis to the outermost point of the beam and I is the second moment of area of the cross section. In this study, the thickness of the hydrofoil profile is $0.12c$, therefore $\hat{z} = 0.06c$.

The coupling of the structural and hydrodynamic models is performed in Python. This allows for a structurally computationally inexpensive analysis and is a powerful evaluation tool that can be used to design large-scale to full-scale LiftWEC prototypes.

IV. Results

A. Tangential and radial forces

Force data, for wave-bladed cyclorotors, is scarce in the literature. Although the LiftWEC consortium will perform an experimental campaign, the data is not available yet. As such, two dimensional numerical simulations force data from Scharmann [33] is utilised here to validate, qualitatively, the outputs of the hydrodynamic model.

The numerical methodology from Scharmann was developed in the commercial solver Ansys CFX and was validated with experimental tests of a laboratory-scale two-bladed cyclorotor device. He then extended

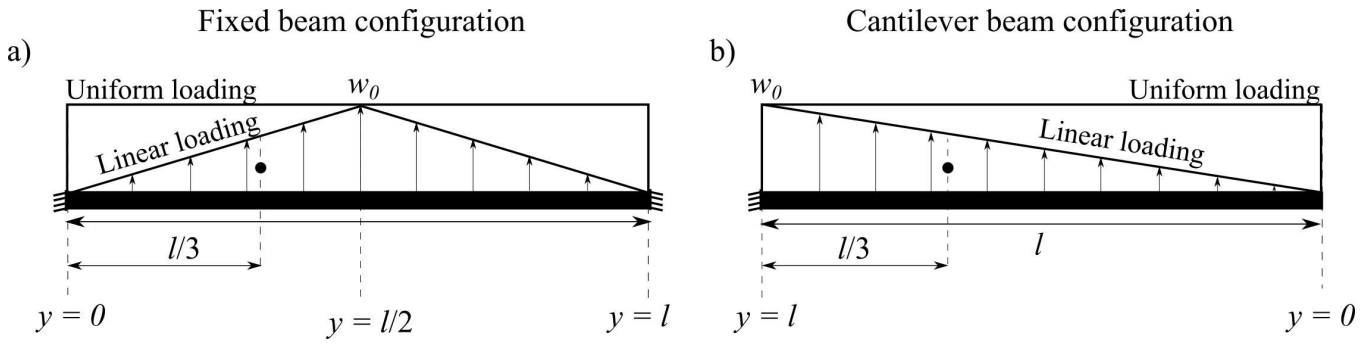

Fig. 7. a) Fixed beam configuration with uniform and linear loading and b) cantilever beam with uniform and linear loading. The maximum distributed load is w_0. The origin of the y-axis is defined in the figures for each configuration.

TABLE II
LINEAR LOADING EQUATIONS FOR V, M AND z FOR FIXED AND CANTILEVER CONFIGURATIONS

	Fixed beam	Cantilever beam
Shear forces V	$V = w_0 l \left(\frac{1}{4} - \frac{y^2}{l^2}\right)$	$V = w_0 \left(\frac{y^2}{2l}\right)$
Bending moments M	$M = w_0 \left(\frac{ly}{4} - \frac{y^3}{3l} - \frac{5l^2}{96}\right)$	$M = w_0 \left(\frac{y^3}{6l}\right)$
Deflections z	$z = \frac{1}{EI}\left(\frac{w_0 l y^3}{24} - \frac{w_0 y^5}{60l} - \frac{5 w_0 l^2 y^2}{192}\right)$	$z = \frac{1}{EI}\left(\frac{w_0 l y^3}{24} - \frac{w_0 y^5}{60l} - \frac{5 w_0 l^2 y^2}{192}\right)$

his numerical methodology to a large-scale device, and compared the results computed with Ansys CFX and OpenFoam. Here, because we are interested in the structural penalty of a large-scale rotor ($r = 10\,\mathrm{m}$, $c = 4\,\mathrm{m}$), we utilise his results for a large-scale device computed in Ansys CFX, which are valid under the assumption of two-dimensional flow.

The wave design parameters used by Scharmann [33] are $T_p = 8$ s and $H = 3$ m. We note that these parameters are different to our wave design parameters specified in Sec. II. The remainder of the rotor parameters are $r = 10$ m and $c = 4$ m. The submergence depth (μ), phase difference ($\Delta\varphi$) and water depth (h) are not specified by Scharman. Here, we make estimates of these parameters. We note that because $H_s = 3\,\mathrm{m}$, in order for the hydrofoils to remain under the through of the wave, the minimum submergence should be $\mu > 3\,\mathrm{m}$. Hence, we set $\mu = 6\,\mathrm{m}$, where $\mu \pm 1$ m does not change the model outputs significantly. Then $h = 50$ m, because we consider intermediate water depths, and deeper water depths ($h > 50$ m) do not change the trends in the modelled results. Whilst $\Delta\varphi = 90°$ is chosen for hydrofoil 1, to set the rotor to the optimum phase. This is further discussed in the next subsection.

Figure 8 shows the comparison of the hydrodynamic model outputs to the results from Scharmann [33]. The figure shows F_T (figure 8a) and F_R (figure 8b) for one normalised period of revolution t/T_p. Results are shown for the two hydrofoils. The model outputs are shown with solid and dotted black lines for hydrofoil 1 and 2, respectively. Scharmann's results are plotted with solid and dotted red lines, for hydrofoils 1 and 2, respectively. In figure2, F_T is plotted considering a local reference frame at the leading-edge of each hydrofoil, where the force is positive pointing outwards of the chord of the foil, as shown in figure 2. In contrast, F_R is defined in the global reference system of the rotor and is defined positive, pointing along the same global direction in both hydrofoils, as shown in figure 2.

In figure 8a, a good match (within 2%) between the predicted and Scharmann's F_{T_2} is seen, whilst the predicted F_{T_1} shows a similar trend to Scharmann's curve but has a different peak magnitude. The maximum amplitude of this peak is about a third of that

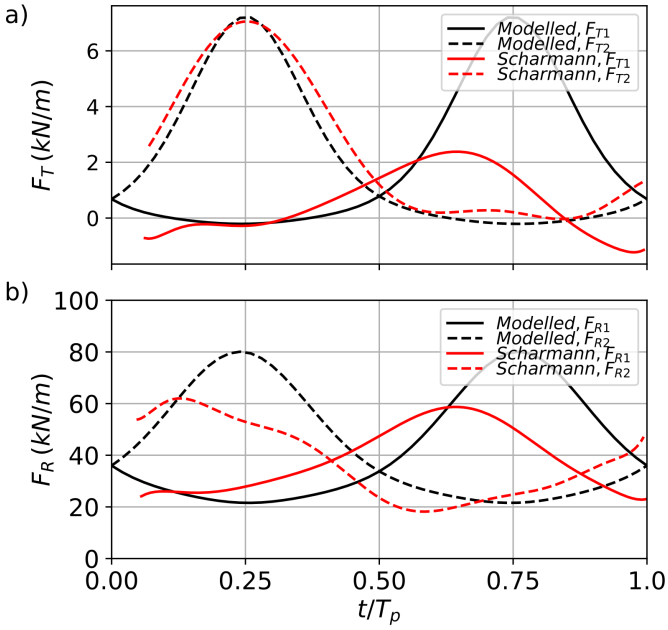

Fig. 8. Tangential (F_T) and radial forces (F_R) computed for hydrofoil 1 and 2 (solid and dotted black lines) of a LiftWEC rotor in one period of rotation (t/T_p), compared to results of two-dimensional numerical simulations by Scharmann [33].

predicted by our current model. Here, the subindices refer to hydrofoil 1 and hydrofoil 2. Figure 8b shows similar trends for F_R, in the two hydrofoils, between Scharmann's results and the current model. With the current model over predicting the maximum amplitude of the loads by about 25%. Discrepancies could be due to unsteady effects that are not accounted for in the hydrodynamic model. The model also does not consider forces on the hydrofoil due to radiated waves, which will have some impact, but these will depend on the width of the hydrofoil [34], [35]. However, we recall that the purpose of this paper is to develop an integral methodology between structural and hydrodynamic models. As such, future refinements to both hydrodynamic and structural models can be included. For the structural analysis, we take a conservative approach and take F_R of hydrofoil 1 computed with the model. We recall that F_R will be the cause of the bending moments and stresses in the hydrofoils.

B. Effect of phase difference ($\Delta\varphi$) in mean power output

In Sec. II, equation 15 shows that the power output (P) depends on F_T and r. In this section, we show the effect of $\Delta\varphi$ on the mean power output $\overline{P}$. This will enable us to calculate the optimal $\Delta\varphi$ of operation. We consider $\Delta\varphi$ for hydrofoil 1, since this also defines $\Delta\varphi$ for hydrofoil 2, as shown in figure 2.

Figure 9 shows $\overline{P}$, computed with the current hydrodynamic model, over a range of $\Delta\varphi$ between -180° to 180°. In the figure, it can be seen that when the rotation of hydrofoil 1 is in phase with the wave, i.e. $\Delta\varphi = 0°$, $\overline{P}$ becomes negative. This means that power is not generated but rather consumed and this is the worst case scenario for the rotor. In contrast, maximum peaks in $\overline{P}$ are obtained when $\Delta\varphi = \pm 90°$. The difference in sign defines the direction of the radial force along the radius of the rotor. Positive sign defines an outwards radial force along the radius of the rotor, whilst negative sign defines an inboard radial force, as shown for example, in figure 2, for hydrofoil 1 and 2, respectively.

We note that the pitch angle of the hydrofoils can significantly increase the mean power capture of LiftWEC. For example, with a pitch angle increase from $0°$ to $5°$, the mean power capture increases from approximately $5\,kW/m$ to about $40\,kW/m$. In fact, according to Siegel [15], a wave bladed cyclorotor of 13 m span could yield about 1 MW of extracted power. However, the scope of this paper does not include any comprehensive discussion on the effect of the pitch angle.

C. Rotor selection: fixed or cantilever beam

The criterion for rotor selection, between fixed and cantilever beam configurations, is presented in this section. Both configurations are shown in figure 5a and figure 5b. The selection criterion is defined in a conservative manner. Firstly, we chose the configuration subject to the lowest maximum bending moment under UL conditions. This is the type of loading that will exert the highest force on the foil. Secondly, we look at the configuration with the lowest variability in bending

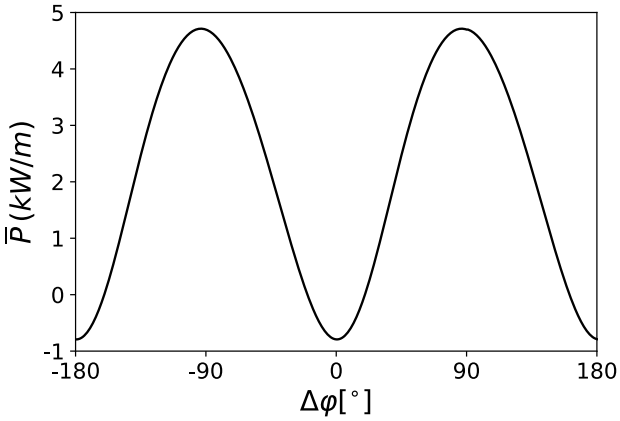

Fig. 9. Mean power output ($\overline{P}$) in kW/m plotted over a range of $\Delta\varphi$ between -180° to 180°, where $\Delta\varphi$ is the phase difference between the rotation of the cyclo-rotor and the incoming wave, as shown in figure 2. The maximum $\overline{P}$ is achieved at $\Delta\varphi = \pm 90°$.

moments when the loading changes from UL to LL. Although large-spanned hydrofoils can promote UL, spanwise flow and eddies due to the unsteadiness of the marine environment can alter and induce a different type of loading. Hence, it is important to minimise this variability and therefore, any cyclic loading and induced failures associated to it.

The solid lines in figure 10 show the bending moments of LiftWEC under UL, whilst the dotted lines show the bending moments for an LL type of loading. The bending moments are plotted during a normalised period (t/T_p). In the figure, the red lines correspond to the cantilever configuration and the black lines to the fixed beam configuration. The maximum bending moments during UL are indicated with circular markers in the figure. The color of the markers follows the same notation as that used for the lines in the figure. It can be seen that, when the hydrofoil is subject to UL, the configuration with the lowest maximum bending moment is the fixed beam configuration.

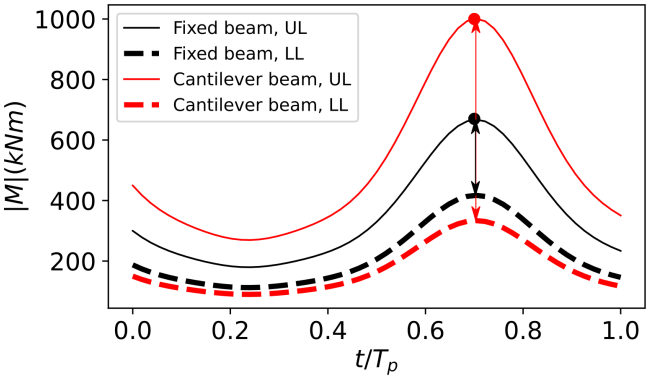

Fig. 10. Maximum bending moment $|M_{max}|$ for fixed and cantilever beam configurations subject to uniform and linear loading during one period of revolution t/T_p.

In terms of variability of bending moments between UL and LL, this is highlighted in figure 10 at the point where the variability is highest. The red vertical

arrow indicates the variability for the cantilever beam configuration, whilst the black vertical arrow indicates the variability for the fixed beam configuration. It is observed that the lowest variability in maximum bending moments occurs in the fixed beam configuration. Based on the above observations, the fixed beam configuration is chosen to size the radius and span of the rotor.

D. Selection of rotor radius and span

The previous section shows that the fixed beam configuration best satisfies our selection criteria: lowest maximum bending moment at UL and lowest variability when the loading changes between UL and LL. In this section, we size the span s and the radius r of the fixed beam configuration rotor, based on σ_a. We recall, from Table I, that $\sigma_a = 117$ MPa. The wave design conditions are $T_p = 10$ s and $H = 4$ m, as specified in Sec. II.

Figure 11 shows the maximum bending stresses ($\hat{\sigma}$) for the fixed beam configuration at UL versus different hydrofoil spans (s). Different radii ranging from 1 to 15 m are plotted with grey dotted lines in intervals of 1 m. The lower and upper boundaries (1 and 15 m) are highlighted with a blue and pink solid lines, respectively. We note that for the tested conditions and $\Delta\varphi = 90°$ in hydrofoil 1, $\overline{P}$ increases with the rotor radius from 1 to 7 m. Thereafter, $\overline{P}$ decreases. These two areas of increasing and decreasing $\overline{P}$ are highlighted in figure 11 in yellow and in pink, respectively. The radius where $\overline{P}$ is maximum is highlighted with a black solid line and is equal to 7 m. The thresholds for σ_a and σ_y are shown with horizontal green and red dotted lines, respectively. We intend to design a rotor whose $\hat{\sigma}$ remains below σ_a, ensuring that the material stays in the elastic range. We compute the distributed load w_0 at the wave design conditions and use this value as the input to the structural model. The span of the device is varied from 0 to 15 m.

Results suggest that the optimum radius to span ratio for the cycloidal rotor is about $r/s \approx 0.8$. This ratio ensures that maximum $\overline{P}$ is extracted, whilst it also ensures that the hydrofoil stresses remain at the allowable stress threshold.

V. Conclusion

This paper presents a methodology for the structural design of LiftWEC. We presented the LiftWEC concept and an efficient hydrodynamic model to estimate the tangential and radial forces of the rotor. We showed the importance of the phase difference ($\Delta\varphi$) between the phase of the incoming wave and that of the rotation of LiftWEC, by displaying the mean power output $\overline{P}$ at different $\Delta\varphi$. The optimum $\Delta\varphi$ is shown to be $\pm 90°$.

Two rotor configurations are analysed, one where the foils of the rotor are supported at the ends (fixed beam) and one where the foils are simply supported in the middle (cantilever beam). We find that the fixed beam configuration encounters a lower maximum bending moment under UL and that for varying loading, the fixed beam configuration undergoes lower variation in maximum bending moments. Hence, the fixed beam configuration is selected as the preferred option to study the effect of the span and the radius size.

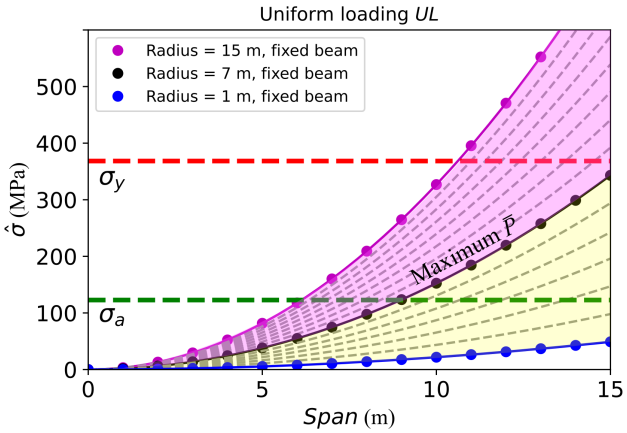

Fig. 11. Maximum bending stresses ($\hat{\sigma}$) versus span (s), at different radii for a fixed beam configuration subject to uniform loading. The radii of the rotor is highlighted at $r = 1$, 7 and 15 m with blue, black and pink solid lines, respectively. Intermediate radii are plotted with dotted grey lines in steps of 1 m. The σ_a and σ_y thresholds are plotted with dotted horizontal green and red lines, respectively. The radius that allows maximum $\overline{P}$ is 7 m.

Our analysis shows, for the wave design tested conditions, the optimum radius to span ratio for the cycloidal rotor is about $r/s \approx 0.8$. This ratio ensures that maximum $\overline{P}$ is extracted, whilst it also ensures that the hydrofoil stresses remain at the allowable stress threshold.

Acknowledgement

LiftWEC is being funded by the European Union's Horizon 2020 Research and Innovation Programme under Grant Agreement No 851885. The authors would like to thank the support and feedback from all of the LiftWEC consortium partners.

References

[1] M. Soede, "Study on lessons for ocean energy development," *European Comission. Final report.*, 2017.

[2] M. J. Pickl, "The renewable energy strategies of oil majors – from oil to energy?" *Energy Strategy Reviews*, vol. 26, p. 100370, 2019.

[3] B. Drew, A. R. Plummer, and M. N. Sahinkaya, "A review of wave energy converter technology," *Proceedings of the Institution of Mechanical Engineers, Part A: Journal of Power and Energy*, vol. 223, no. 8, pp. 887–902, 2009.

[4] M. Lehmann, F. Karimpour, C. A. Goudey, P. T. Jacobson, and M.-R. Alam, "Ocean wave energy in the United States: Current status and future perspectives," *Renewable and Sustainable Energy Reviews*, vol. 74, pp. 1300 – 1313, 2017.

[5] P. Schmitt, T. Whittaker, D. Clabby, and K. Doherty, "The opportunities and limitations of using CFD in the development of wave energy converters," in *RINA, Royal Institution of Naval Architects - International Conference on Marine and Offshore Renewable Energy 2012*, 2012, pp. 89–97.

[6] I. H. Abbot and A. E. Doenhoff, *Theory of wing sections: including a summary of airfoil data*, 1st ed. Dover Publications, Inc., 1959.

[7] A. C. Hansen and C. P. Butterfield, "Aerodynamics of horizontal-axis wind turbines," *Annual Review of Fluid Mechanics*, vol. 25, no. 1, pp. 115–149, 1993.

[8] G. T. Scarlett, B. Sellar, T. van den Bremer, and I. M. Viola, "Unsteady hydrodynamics of a full-scale tidal turbine operating in large wave conditions," *Renewable Energy*, vol. 143, pp. 199 – 213, 2019.

[9] J. G. Leishman, "Principles of helicopter aerodynamicsr," *Cambridge University Press*, 2002.
[10] S. A. Kinnas and C.-Y. Hsin, "Boundary element method for the analysis of the unsteady flow aroundextreme propeller geometries," *AIAA Journal*, vol. 30, no. 3, pp. 688–696, 1992.
[11] A. Hermans, E. Van Sabben, and J. Pinkster, "A device to extract energy from water waves," *Applied Ocean Research*, vol. 12, no. 4, pp. 175 – 179, 1990.
[12] J. A. Pinkster and A. J. Hermans, "A rotating wing for the generation of energy from waves," in *the 22nd IWWWFB conference*, 2007.
[13] J. Chaplin and C. Retzler, "Predictions of the hydrodynamic performance of the wave rotor wave energy device," *Applied Ocean Research*, vol. 17, no. 6, pp. 343 – 347, 1995.
[14] S. G. Siegel, T. Jeans, and T. McLaughlin, "Intermediate Ocean Wave Termination Using a Cycloidal Wave Energy Converter," in *International Conference on Offshore Mechanics and Arctic Engineering*, 06 2010, pp. 293–301.
[15] S. Siegel, T. Jeans, and T. McLaughlin, "Deep ocean wave energy conversion using a cycloidal turbine," *Applied Ocean Research*, vol. 33, no. 2, pp. 110 – 119, 2011.
[16] J. T. Imamura, S. G. Siegel, C. Fagley, and T. McLaughlin, "Cancellation of Non-Harmonic Waves Using a Cycloidal Turbine," in *International Conference on Offshore Mechanics and Arctic Engineering*, 06 2011, pp. 385–393.
[17] T. Jeans, C. Fagley, S. Siegel, and J. Seidel, "Irregular deep ocean wave energy attenuation using a cycloidal wave energy converter," *International Journal of Marine Energy*, vol. 1, pp. 16 – 32, 2013.
[18] C. P. Fagley, J. J. Seidel, and S. G. Siegel, "Computational Investigation of Irregular Wave Cancelation Using a Cycloidal Wave Energy Converter," in *International Conference on Offshore Mechanics and Arctic Engineering*, 07 2012, pp. 351–358.
[19] C. Fagley, S. G. Siegel, J. Seidel, and C. Schmittner, "3D Efficiency Analysis of Cycloidal Wave Energy Converters in Oblique Wave Fields," in *International Conference on Offshore Mechanics and Arctic Engineering*, 06 2013.
[20] S. Siegel, "Wave radiation of a cycloidal wave energy converter," *Applied Ocean Research*, vol. 49, pp. 9 – 19, 2015.
[21] S. G. Siegel, "Numerical benchmarking study of a cycloidal wave energy converter," *Renewable Energy*, vol. 134, pp. 390 – 405, 2019.
[22] M. Folley and T. Whittaker, "Lift-based wave energy converters – an analysis of their potential," in *13th European Wave and Tidal Energy Conference*, 2019.
[23] J. P. Sierra, A. White, C. Mösso, and M. Mestres, "Assessment of the intra-annual and inter-annual variability of the wave energy resource in the bay of biscay (france)," *Energy*, vol. 141, pp. 853 – 868, 2017. [Online]. Available: http://www.sciencedirect.com/science/article/pii/S0360544217316328
[24] T. Burton, J. N., and Sharpe, *Wind Energy Handbook*, 2nd ed. Wiley, 2011.
[25] G. B. Airy, *Tides and waves*. Encyc. Metro., 1985, no. 192.
[26] M. McCormick, *Ocean wave energy conversion*, dover edition ed. Dover Publications Inc, 2013.
[27] R. E. Sheldahl and P. C. Klimas, "Aerodynamic characteristics of seven symmetrical airfoil sections through 180-degree angle of attack for use in aerodynamic analysis of vertical axis wind turbines," *Sandia National Laboratories.*, 3 1981.
[28] F. Brennan and I. Tavares, "Fatigue design of offshore steel mono-pile wind substructures," ser. Proceedings of the Institution of Civil Engineers Energy, vol. Volume 167 Issue EN4, 11 2014.
[29] R. M. Ajaj, M. I. Friswell, D. Smith, and A. T. Isikveren, "A conceptual wing-box weight estimation model for transport aircraft," *The Aeronautical Journal*, vol. 117, no. 1191, p. 533–551, 2013.
[30] W. Phillips, D. Hunsaker, and J. Taylor, "Minimising induced drag with weight distribution, lift distribution, wingspan, and wing-structure weight," *The Aeronautical Journal*, vol. 124, no. 1278, p. 1208–1235, 2020.
[31] J. Hulse, R.; Cain, *Structural Mechanics*, 2nd ed. Red Globe Press, 2000.
[32] W. C. Young, R. G. Budynas, and A. M. Sadegh, *Roark's Formulas for Stress and Strain, Eighth Edition*, 8th ed. New York: McGraw-Hill Education, 2012. [Online]. Available: https://www.accessengineeringlibrary.com/content/book/9780071742474
[33] N. Scharmann, "Ocean energy conversion systems: The wave hydro-mechanical rotary energy converter," *PhD thesis*, 2014.
[34] P. Lamont-Kane, M. Folley, C. Frost, and T. Whittaker, "A methodology for the structural design of LiftWEC: A wave-bladed cyclorotor," ser. Proceedings of the 14th European Wave and Tidal Energy Conference, 2021.
[35] A. Ermakov and J. V. Ringwood, "A control-orientated analytical model for a cyclorotor wave energy device with n hydrofoils," *Journal of Ocean Engineering and Marine Energy*, vol. 7, no. 2, pp. 201–210, May 2021.